



Analysis of the dissipation and dispersion properties of the multi-domain Chebyshev pseudospectral method



D. Dagna^{a,*}, C. Bogey^a, M. Hornikx^b, P. Blanc-Benon^a

^a Laboratoire de Mécanique des Fluides et d'Acoustique, UMR CNRS 5509, Ecole Centrale de Lyon, Université de Lyon, 69134 Ecully Cedex, France

^b Building Physics and Services, Eindhoven University of Technology, PO Box 513, 5600 MB Eindhoven, The Netherlands

ARTICLE INFO

Article history:

Received 10 December 2012

Received in revised form 26 July 2013

Accepted 30 July 2013

Available online 17 August 2013

Keywords:

Chebyshev pseudospectral method

Wave propagation

Multi-domain method

ABSTRACT

The accuracy of the multi-domain Chebyshev pseudospectral method is investigated for wave propagation problems by examining the properties of the method in the wavenumber space theoretically in terms of dispersion and dissipation errors. For a number of $(N + 1)$ points in the subdomains used in the literature, with N typically between 8 to 32, significant errors can be obtained for waves discretized by more than π points per wavelength. The dispersion and dissipation errors determined from the analysis in the wavenumber space are found to be in good agreement with those obtained in test cases. Accuracy limits based on arbitrary criteria are proposed, yielding minimum resolutions of 7.7, 5.2 and 4.0 points per wavelength for $N = 8, 16$ and 32 respectively. The numerical efficiency of the method is estimated, showing that it is preferable to choose N between 16 and 32 in practice. The stability of the method is also assessed using the standard fourth-order Runge–Kutta algorithm. Finally, 1-D and 2-D problems involving long-range wave propagation are solved to illustrate the dissipation and dispersion errors for short waves. The error anisotropy is studied in the 2-D case, in particular for a hybrid Fourier–Chebyshev configuration.

© 2013 Elsevier Inc. All rights reserved.

1. Introduction

Long-range wave propagation problems require accurate numerical differentiation schemes, which must generate very low dispersion and dissipation errors. Among the available methods, pseudospectral (PS) methods are well-established approaches [1], and have been extensively used for wave propagation problems in time domain in several fields of physics (see Refs. [2–7]). Using pseudospectral methods, contrary to finite-difference methods, the derivative of a variable at a single point is computed from its values at all grid points [8]. Two types of pseudospectral methods are usually distinguished. For periodic problems, Fourier PS methods are generally used, with equally spaced collocation points. The accuracy is however poor for non-periodic problems, due to Gibbs oscillations [8]. In that case, PS methods based on the Chebyshev polynomials or other orthogonal polynomials are preferred. For these methods, the collocation points, which are usually chosen as the Gauss–Lobatto points, are unevenly spaced.

Despite their wide use, little is known about the properties of the pseudospectral methods in the wavenumber space. They are particularly of interest when the number of grid points $(N + 1)$ is small. Indeed, for PS methods, the differentiation error for well-behaved functions [9] decreases exponentially with the number of points. For Fourier PS method, the

* Corresponding author.

E-mail addresses: didier.dagna@ec-lyon.fr (D. Dagna), christophe.bogey@ec-lyon.fr (C. Bogey), m.c.j.hornikx@tue.nl (M. Hornikx), philippe.blanc-benon@ec-lyon.fr (P. Blanc-Benon).

parameter N takes large values in applications, typically greater than 128 (e.g. see [10,11]), ensuring a satisfactory accuracy for waves down to two points per wavelength, which corresponds to the limitation of the Nyquist–Shannon sampling theorem. For Chebyshev PS method, due to the non-uniform grid, accuracy is satisfactory for large N only for waves discretized down to π points per wavelength (e.g. see [9]). Moreover, the distribution of the Gauss–Lobatto collocation points implies that the minimum grid size decreases quadratically with increasing N , which can lead to severe restriction on the time step when using explicit time-integration methods. For wave propagation applications, it is thus common to split the domain into subdomains to relax the time step limitation [12–14]. The number of points ($N + 1$) in each subdomain can take low values, with N typically between 8 and 32. For such values, the numerical error is expected to be significant for short wavelengths.

The main objective of this paper is to study the numerical errors introduced by the multi-domain PS Chebyshev method in the wavenumber space. The corollary is to provide accuracy limits, on which future work could rely. In the literature, similar studies have been performed concerning the spectral element method by Hu et al. [15], Gassner and Kopriva [16] and Melvin et al. [17]. This method differs from the multi-domain pseudospectral method by the use of the variational principle [8]. Numerical errors have also been investigated for two other spectral methods, which are the spectral difference method [18] and the spectral volume method [19]. However, few studies have been devoted to the multi-domain pseudospectral approach. One can mention for instance the work of Kopriva [20], in which the convection of a 1-D wave has been examined. It has been shown that the dispersion and dissipation errors, which are respectively the error on the phase and on the amplitude of the computed wave, both decrease exponentially with the number of points. Besides, Wasberg and Gottlieb [21] have carried out an analysis on the optimal decomposition for a multi-domain spectral method. However, that work is based on the truncation error of the Chebyshev expansion of the sine function and does not take into account interface treatment that plays a role on the accuracy of the method. All these studies show that significant errors are generated for waves close to the limit of π points per wavelength, in particular for small values of N . For instance, Boyd [8] suggested as a rule-of-thumb to use a resolution of 3.5 points per wavelength to reach a 5% accuracy. However, no systematic study of the typical number of points per wavelength required to obtain accurate solutions at long range for wave propagation problems has been proposed in the literature. This is one of the objectives in this paper.

For finite-difference methods, the dispersion and dissipation properties of the numerical schemes have been quantified in a number of studies [22–24]. For that, the eigenfunctions of the first derivative finite-difference operator, which are the Fourier modes $u(x) = \exp(ikx)$, are considered. The associated eigenvalues are denoted by ik^* , where k^* is referred to as the effective wavenumber. A comparison can then be made with the exact eigenvalues ik of the derivative operator. In the present study, the eigenvalues of the multi-domain Chebyshev PS derivative operator for the 1-D advection equation are investigated. A theoretical analysis is carried out to determine the dispersion and dissipation errors. The obtained values are compared to those estimated in test cases. The paper is organized as follows. In Section 2, the effective wavenumber obtained using the multi-domain Chebyshev PS method is introduced. The dispersion and dissipation errors are discussed depending on the value of N , and accuracy limits are proposed. The stability of the method is assessed, using the standard fourth-order Runge–Kutta algorithm. Several test cases are resolved to verify the theoretical analysis. In Section 3, applications of the multi-domain Chebyshev PS methods are performed to illustrate the previous study. In particular, a multi-dimensional problem is considered to examine the variations of the errors with the direction of wave propagation.

2. Analysis of the Chebyshev PS method in the wavenumber space

In the same way as in the studies performed by Hu et al. [15] and Gassner and Kopriva [16] for the discontinuous Galerkin spectral element method, the 1-D advection equation for a variable p is considered:

$$\frac{1}{c} \frac{\partial p}{\partial t} + \frac{\partial p}{\partial x} = 0 \quad (1)$$

where c is the propagation speed. The equation is solved on a numerical domain divided into subdomains $I_l = [x_l, x_{l+1}]$ of uniform length $\delta = x_{l+1} - x_l$. The spatial derivative is approximated using the Chebyshev pseudospectral derivative operator. For a given subdomain, the coordinate transformation:

$$x(\xi) = \frac{(x_{l-1} + x_l)}{2} + \frac{\delta}{2}\xi \quad (2)$$

is introduced to scale the problem to the interval $[-1, 1]$. On each subdomain, the solution is discretized on the $(N + 1)$ Gauss–Lobatto points located at $\xi_i = -\cos(i\pi/N)$, for $0 \leq i \leq N$. The average mesh size is $\Delta = \delta/N$. At the interfaces, conditions are imposed to transfer information through the subdomains. Denoting by p^- and p^+ the respective values of p at the left and right hand sides of an interface, the boundary conditions are written as a linear combination:

$$p^\pm = (1 - \gamma)p^+ + \gamma p^- \quad (3)$$

with γ a real number between 0 and 1. In particular, the case $\gamma = 1$ corresponds to the method of the characteristics. Using matrix-vector notation leads to the following equation on the subdomain I_l :

$$\frac{\delta}{2c} \frac{\partial p|_{I_l}}{\partial t} + \mathbf{D}p|_{I_l} + \mathbf{E}p|_{I_{l-1}} + \mathbf{F}p|_{I_{l+1}} = 0 \quad (4)$$

where the matrix \mathbf{D} contains the information of the subdomain I_l and the matrices \mathbf{E} and \mathbf{F} provide the information from the left and the right adjacent subdomains, respectively. The matrix \mathbf{D} is closely related to the Chebyshev differentiation matrix \mathbf{C} with $C_{ij} = (l_j)_\xi(\xi_i)$ [9], where $(l_j)_{0 \leq j \leq N}$ denotes the Lagrange interpolating polynomials associated with the Gauss–Lobatto points. For the interior points $0 \leq i \leq N$ and $1 \leq j \leq (N-1)$, one obtains $D_{ij} = C_{ij}$. At the boundary points, based on (3), the rows of the matrix are equal to $D_{i0} = (1 - \gamma)C_{i0}$ and $D_{iN} = \gamma C_{iN}$, for $0 \leq i \leq N$. Concerning the matrices \mathbf{E} and \mathbf{F} , all the rows are null except for the boundary points, yielding $E_{iN} = \gamma C_{i0}$ and $F_{i0} = (1 - \gamma)C_{iN}$, for $0 \leq i \leq N$.

A harmonic-wave type solution is now considered:

$$p(\xi, t)|_{I_l} = \hat{p}(\xi) \exp(ikl\delta - i\omega t) \quad (5)$$

for a wavenumber k and an angular frequency ω . Time integration is here assumed to generate no error. Introducing solution (5) into Eq. (4) provides:

$$\frac{-i\tilde{k}\delta}{2}\hat{p} + \mathbf{D}\hat{p} + \exp(-ik\delta)\mathbf{E}\hat{p} + \exp(+ik\delta)\mathbf{F}\hat{p} = 0 \quad (6)$$

with $\tilde{k} = \omega/c$. In the following, the average mesh size Δ is used as the reference length scale instead of δ . The eigenvalue problem $\mathbf{A}(k\Delta)\hat{p} = \tilde{k}(k\Delta)\Delta\hat{p}$ is obtained, with the matrix:

$$\mathbf{A}(k\Delta) = -2iN[\mathbf{D} + \exp(-ik\Delta N)\mathbf{E} + \exp(+ik\Delta N)\mathbf{F}] \quad (7)$$

For a given value of N , the eigenvalues and the eigenmodes depend on the wavenumber k , as well as the conditions at the interfaces, hence on γ . The first and last columns of matrix \mathbf{A} are linearly dependent, because the same values are imposed at both sides of the interfaces. Consequently, for a given value of $k\Delta$, there is a maximum of N non-zero eigenvalues \tilde{k} , corresponding to numerical wavenumbers associated with the N modes.

Some properties of the wavenumbers of the modes can be deduced from the expression of matrix \mathbf{A} . First, if the complex conjugate of matrix \mathbf{A} is denoted by $\bar{\mathbf{A}}$, the relation $\bar{\mathbf{A}}(k\Delta) = -\mathbf{A}(-k\Delta)$ is found. This implies that the set of wavenumbers obtained for $-k\Delta$ is related to that obtained for $k\Delta$ by $\tilde{k}(-k\Delta) = -\tilde{k}(k\Delta)$. Secondly, since the matrix \mathbf{A} depends only on $\exp(\pm ik\Delta N)$, the matrix is periodic as a function of $k\Delta$ of period $2\pi/N$. As a result, the spectrum of the matrix $\mathbf{A}(k\Delta)$ is also periodic of period $2\pi/N$, hence:

$$\tilde{k}\left(k\Delta + \frac{2\pi}{N}\right) = \tilde{k}(k\Delta) \quad (8)$$

In what follows, the method of the characteristics is used at the interfaces of the subdomains. As proposed by Hu et al. [15], the physical mode is defined as the mode whose wavenumber best approximates the exact dispersion relation $\tilde{k} = k$ over a non-trivial range of wavenumbers. The wavenumber associated with the physical mode is referred to as the effective wavenumber and is denoted by k^* . The other modes are considered as numerical modes.

An analytical expression for k^* can be obtained for $N = 1$ and for $N = 2$. For $N = 1$, the effective wavenumber is:

$$k^*\Delta = \sin(k\Delta) - i(1 - \cos(k\Delta)) \quad (9)$$

which corresponds to the effective wavenumber of the first-order upwind finite-difference scheme. For $N = 2$, the expression of the effective wavenumber for $k\Delta \in [0, \pi]$ is:

$$k^*\Delta = \frac{\sqrt{7 - 22\exp(-2ik\Delta) - \exp(-4ik\Delta)}}{4} - i\left(\frac{3 + \exp(-2ik\Delta)}{4}\right) \quad (10)$$

Based on a Taylor expansion of $k^*\Delta$ around $k\Delta = 0$, it can thus be shown that the multi-domain Chebyshev PS method is third-order accurate for $N = 2$. It can also be noted that the expression for the effective wavenumber in (10) does not correspond to that of any finite-difference scheme, which is written as a sum of sine and cosine functions. For $N \geq 3$, the effective wavenumber is determined numerically. Fig. 1 shows the real and imaginary parts of the wavenumbers of the modes obtained for $N = 4$ as functions of the exact wavenumber $k\Delta$. The effective wavenumber is clearly distinct from the wavenumbers associated with the numerical modes. In particular, for small values of $|k\Delta|$, its real part is superimposed on the line $\text{Re}(\tilde{k})\Delta = k\Delta$ and its imaginary part is very close to zero.

The effective wavenumber shows other particular properties. First, it satisfies $k^*(-k\Delta) = -\overline{k^*(k\Delta)}$ for all values of N . The real part of k^* is then antisymmetric, and its imaginary part is symmetric. This is seen for the case $N = 4$ in Fig. 1. Moreover, for $N \leq 51$, it is observed that $k^*(k\Delta)$ is a periodic function with period 2π . For $N = 52$ to $N = 256$, $k^*(k\Delta)$ is still periodic but with a smaller period, equal to $2\pi(N-2)/N$. As an example, the real and imaginary parts of the wavenumbers of different modes are shown in Fig. 2 for $N = 52$ as functions of the exact wavenumber $k\Delta$. As for $N = 4$, for small values of $|k\Delta|$, the real part of the effective wavenumber is superimposed on the line $\text{Re}[\tilde{k}\Delta] = k\Delta$ and its imaginary part is very close to zero. It appears also that the period of $k^*\Delta$ is smaller than 2π . In all cases, it is thus sufficient to consider the real and imaginary parts of $k^*\Delta$ on the interval $k\Delta \in [0, \pi]$.

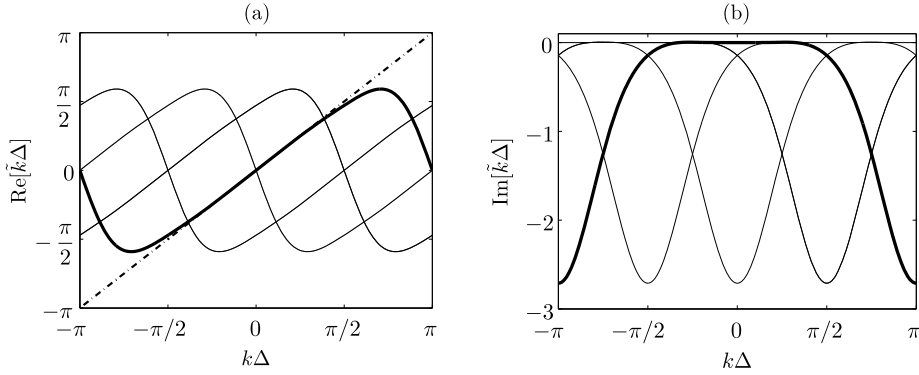


Fig. 1. (a) Real and (b) imaginary parts of the wavenumbers $\tilde{k}\Delta$ of the modes obtained for $N=4$ as functions of the exact wavenumber $k\Delta$: — effective wavenumber and — wavenumbers associated with the numerical modes.

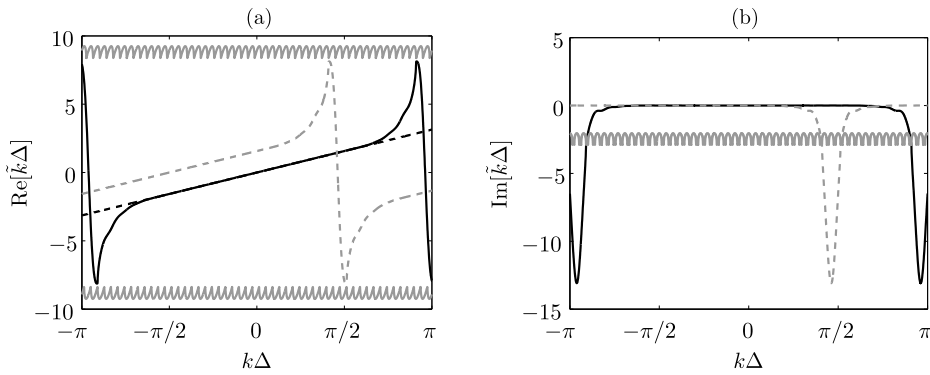


Fig. 2. (a) Real and (b) imaginary parts of the wavenumbers $\tilde{k}\Delta$ of different modes obtained for $N=52$ as functions of the exact wavenumber $k\Delta$: — effective wavenumber, — $2\pi/N$ -periodic numerical wavenumbers and - - an example of numerical wavenumber corresponding to the effective wavenumber shifted along the $k\Delta$ -axis.

Concerning the numerical modes, for $N \leq 51$, their wavenumbers correspond to the effective wavenumber shifted along the $k\Delta$ -axis by multiples of $2\pi/N$. This is the case in Fig. 1 for $N=4$, where the shift is equal to $\pi/2$. From $N=52$ to $N=256$, two modes are distinct from the other ones. Their wavenumbers are periodic with period $2\pi/N$, and have the largest real parts among all numerical wavenumbers. This is observed in Fig. 2 for $N=52$. It is also found that one of these two wavenumbers has positive real parts, whereas the second one has negative real parts. Their imaginary parts are large, with $\text{Im}[\tilde{k}\Delta] < -2$, over the whole range of wavenumbers. For the other modes, $\tilde{k}(k\Delta)$ corresponds to the effective wavenumber k^* shifted along the $k\Delta$ -axis by multiples of $2\pi/N$. An example is displayed in Fig. 2 for $N=52$ with a shift equal to $\pi/2$.

2.1. Dispersion error

The error related to the phase, namely the dispersion error, is characterized by plotting the real part of the effective wavenumber in Fig. 3(a) as a function of the exact wavenumber $k\Delta$ for different values of N , between $N=2$ and $N=128$. For low wavenumbers, typically $k\Delta < \pi/4$, all curves are superimposed on the line $\text{Re}[k^*\Delta] = k\Delta$. For higher wavenumbers, the curves begin to deviate from this line at different values. As an example, the error $|\text{Re}(k^*)\Delta - k\Delta|$ becomes larger than 1% for $k\Delta = 1.4$ for $N=8$, and for $k\Delta = 1.86$ for $N=16$. For $N > 16$, the relation $\text{Re}[k^*\Delta] = k\Delta$ is nearly satisfied up to $k\Delta = 2$. For $k\Delta > 2$, the errors are however large even with increasing N . This limit of $k\Delta = 2$ corresponds to the classical restriction of π points per wavelength for the Chebyshev PS method [9]. The variations of $\text{Re}[k^*\Delta]$ close to $k\Delta = \pi$ are finally shown in Fig. 3(b). A large overshoot increasing with N is observed. This behavior has previously been found for discontinuous Galerkin spectral element methods in [15] and [16].

Fig. 4 displays the dispersion error given by $|\text{Re}(k^*\Delta) - k\Delta|/\pi$. At low wavenumbers, the dispersion error is significant for small values of N . For instance, for $N=4$, it is higher than 10^{-5} for $k\Delta > \pi/10$. Increasing N leads to a considerable reduction of the dispersion error for small $k\Delta$. Thus, for values of N larger than 32, it is lower than 10^{-5} up to $k\Delta = \pi/2$. Finally, the dispersion error is important for $k\Delta > 2$ for all values of N .

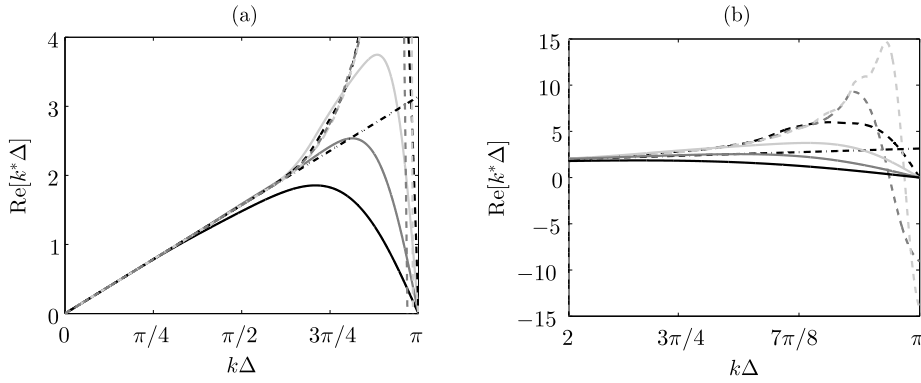


Fig. 3. (a) Real part of the effective wavenumber $k^*\Delta$ as a function of the exact wavenumber $k\Delta$ and (b) view on the overshoots for $k\Delta \in [2; \pi]$, for — $N=4$, — $N=8$, — $N=16$, -- -- $N=32$, -- -- $N=64$ and -- -- $N=128$.

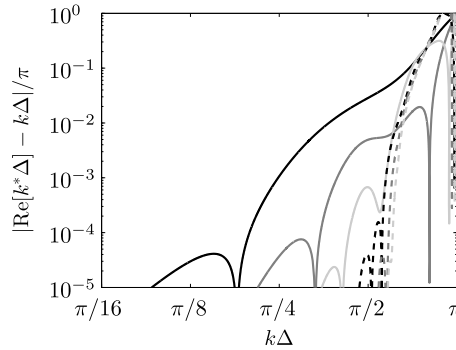


Fig. 4. Dispersion error $|\text{Re}(k^*\Delta) - k\Delta|/\pi$ as a function of the exact wavenumber $k\Delta$, obtained for — $N=4$, — $N=8$, — $N=16$, -- -- $N=32$, -- -- $N=64$ and -- -- $N=128$.

2.2. Dissipation error

The dissipation error, which is the error on the amplitude of the solution, results from the imaginary part of the effective wavenumber. In Fig. 5(a), the imaginary part of $k^*\Delta$ is plotted as a function of the exact wavenumber for different values of N . It is close to zero for small wavenumbers, and takes negative values decreasing when $k\Delta$ increases. It is significant for the case $N=8$ from $k\Delta = \pi/3$. In addition, $\text{Im}[k^*\Delta]$ is close to zero over a broader range of wavenumbers with increasing N . Fig. 5(b) shows the values of $\text{Im}[k^*\Delta]$ for $k\Delta$ between 2 and π . As observed for $\text{Re}[k^*\Delta]$ in Fig. 3(b), the imaginary part of the effective wavenumber is large near $k\Delta = \pi$ for all values of N , and its minimum value decreases with increasing N .

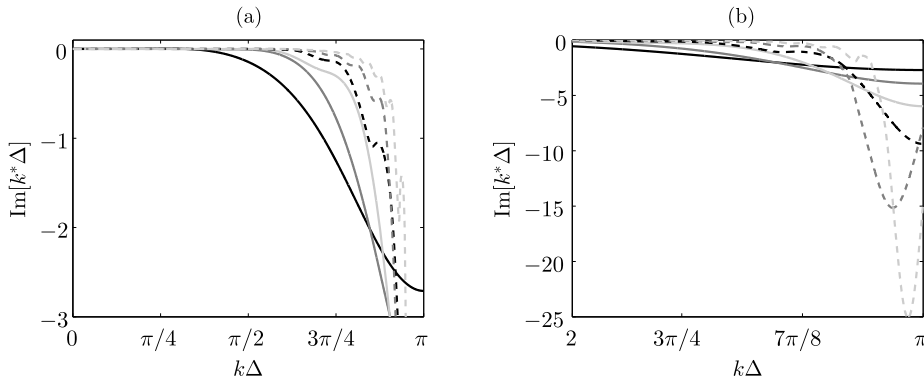


Fig. 5. (a) Imaginary part of the effective wavenumber $k^*\Delta$ as a function of the exact wavenumber $k\Delta$, and (b) view on the interval $k\Delta \in [2, \pi]$, for — $N=4$, — $N=8$, — $N=16$, -- -- $N=32$, -- -- $N=64$ and -- -- $N=128$.

For $N \geq 3$, the imaginary part of $\text{Im}[k^*\Delta]$ is positive over a narrow range of wavenumbers, as is observed in Fig. 6. For $N=4$, for example, this is the case approximately over $\pi/8 \leq k\Delta \leq 3\pi/8$. Waves whose wavenumbers lie in this range are consequently amplified. The maximum values of $\text{Im}[k^*\Delta]$ are however small, typically lower than 5×10^{-3} , yielding low

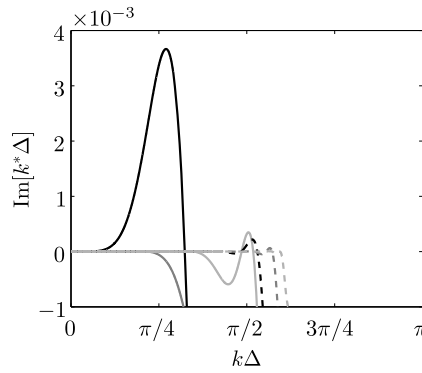


Fig. 6. Close-up on the positive values of the imaginary part of the effective wavenumber $k^*\Delta$, as a function of the exact wavenumber $k\Delta$, for — $N = 4$, — $N = 8$, — $N = 16$, - - $N = 32$, - - $N = 64$ and - · - $N = 128$.

amplification rates. Moreover, it is observed that the maximum value of $\text{Im}[k^*\Delta]$ decreases generally with increasing N . It is equal to 2×10^{-4} for $N = 32$, 6×10^{-5} for $N = 64$ and 5×10^{-6} for $N = 128$. The amplification due to the positive value of $\text{Im}[k^*\Delta]$ implies some stability issues which are discussed in Section 2.5.

Fig. 7 shows the dissipation error, given by the relation $|1 - \exp[\text{Im}(k^*\Delta)]|$, as a function of the exact wavenumber $k\Delta$. As expected, the dissipation error decreases with increasing N . For $N < 8$, it takes significant values for small wavenumbers. For instance, for $N = 4$, the dissipation error is larger than 10^{-5} for $k\Delta > \pi/13$. For values of N greater than 32, it is smaller than 10^{-5} up to $k\Delta = \pi/2$, which is comparable to values obtained for the dispersion error. Furthermore, as for the dispersion errors, the dissipation errors are large for $k\Delta > 2$ and do not decrease notably with increasing N in that particular range of wavenumbers.

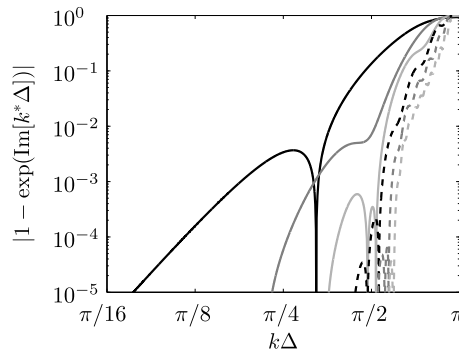


Fig. 7. Dissipation error $|1 - \exp(\text{Im}(k^*\Delta))|$ as a function of the exact wavenumber $k\Delta$, for — $N = 4$, — $N = 8$, — $N = 16$, - - $N = 32$, - - $N = 64$ and - · - $N = 128$.

2.3. Test cases

In this section, the 1-D advection equation (1) is solved using the multi-domain Chebyshev PS method. Results are compared with those obtained theoretically above. An initial value problem is considered, with an initial solution $p(x, t = 0) = \exp(ikx)$, which can be expanded, on a subdomain I_l , as a sum of the eigenmodes V_m :

$$p(x, t = 0)|_{I_l} = \exp(ikx)|_{I_l} = \sum_{m=1}^N \lambda_m V_m(k, x) \quad (11)$$

where λ_m are expansion coefficients. Denoting by \tilde{k}_m the wavenumber associated with the eigenmode V_m , the solution of the problem reads [15]:

$$p(x, t)|_{I_l} = \sum_{m=1}^N \lambda_m V_m(k, x) \exp(-i\tilde{k}_m c t) \quad (12)$$

Thus, the solution corresponds to a sum of exponentially decaying or increasing functions with time. At long time, the eigenmode whose wavenumber has the largest imaginary part is dominant.

In what follows, the propagation speed is equal to $c = 1$. The numerical solution is advanced to $t = 120\Delta$, where Δ denotes the average mesh size, using the six-stage fourth-order Runge–Kutta algorithm of Berland et al. [25] for time

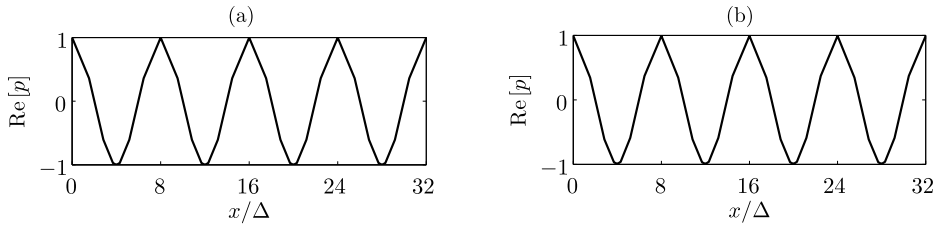


Fig. 8. Real part of the numerical solution for $k\Delta = \pi/4$ and for $N = 8$ as a function of x/Δ (a) at $t = 0$ and (b) at $t = 120\Delta$.

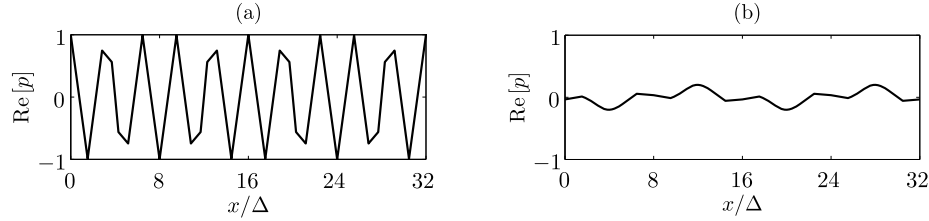


Fig. 9. Real part of the numerical solution for $k\Delta = 5\pi/8$ and for $N = 8$ as a function of x/Δ (a) at $t = 0$ and (b) at $t = 120\Delta$.

integration. The time step is chosen as 0.05Δ in order to generate negligible time-integration errors. The parameter N related to the number of points in the subdomains ($N + 1$) is set to $N = 8$. The changes of the variable p between the initial time and the final time depending on the value of $k\Delta$ are highlighted in Figs. 8 and 9 for initial waves with $k\Delta = \pi/4$ and $5\pi/8$, respectively. In the first case, for $k\Delta = \pi/4$, the numerical solution at the final time shows little dissipation and dispersion. This can be related to the theoretical values of the dispersion and dissipation errors which are small, lower than 10^{-4} , as seen in Figs. 4 and 7. Here, the leading mode is the physical mode. In the second case, for $k\Delta = 5\pi/8$, the solution at the final time has a much smaller amplitude and a larger wavelength than the initial solution, suggesting that the leading mode is not the physical mode. To support this claim, it can be noticed that, as visible in Fig. 5(a), the imaginary part of the effective wavenumber has a large value for $k\Delta = 5\pi/8$ and $N = 8$, i.e. $\text{Im}[k^*\Delta] = -0.12$, which implies that the physical mode is strongly attenuated at $t = 120\Delta$. Therefore, the leading mode corresponds in this case to a numerical mode.

Calculations are now performed for wavenumbers over the range $k\Delta \in [0, \pi]$. From (12), assuming that there is a leading mode at long time, the numerical solution can be expressed as $p(x, t) = \lambda V(k, x) \exp(-ikct)$. The real and imaginary parts of the wavenumber of the leading mode can be deduced from the time variations of the phase and of the amplitude of the solution with:

$$\arg[p(x, t)] \propto -\text{Re}[\tilde{k}]t \quad (13)$$

$$\log|p(x, t)| \propto \text{Im}[\tilde{k}]t \quad (14)$$

Thus, the solution is recorded at a single grid point in the numerical domain from $t = 80\Delta$ to $t = 120\Delta$. Using a least squares approach, the phase and the logarithm of the amplitude of the solution are fitted by lines. From (13) and (14), the real and the imaginary parts of the wavenumber of the leading mode are then estimated from the slopes of the two lines. As an example, the time variations of the phase of p and of the logarithm of $|p|$ are displayed in Fig. 10 for an initial wave with wavenumber $k\Delta = \pi/4$, for which the solutions at the initial and final times are shown in Fig. 8. It is

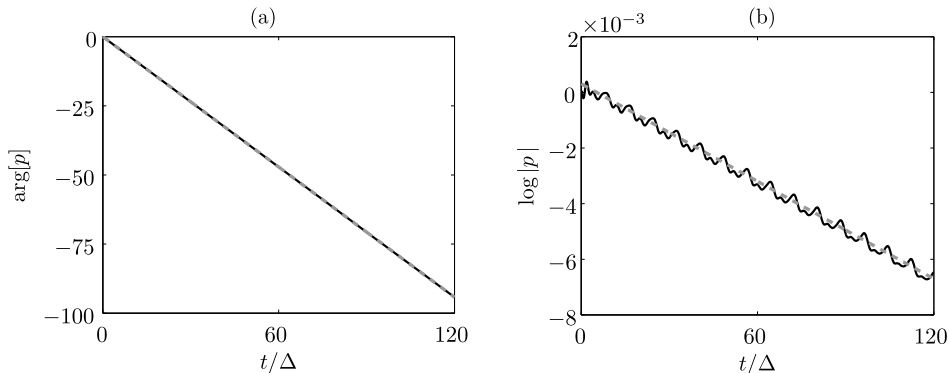


Fig. 10. Time variations of (a) the phase of p and (b) of the logarithm of $|p|$ for $k\Delta = \pi/4$ and for $N = 8$: — numerical solution and - - linear regression line.

observed that $\arg(p)$ and $\log|p|$ are well approximated by lines over the whole simulation period. The estimation of the real part of the wavenumber from the slope of the linear regression line in Fig. 10(a) gives $\text{Re}(\tilde{k}\Delta) = \pi/4$, which is equal to the initial wavenumber. Indeed, for this small wavenumber, the dispersion error is very low, and is about 4×10^{-5} , as observed in Fig. 4 for $N = 8$ and $k\Delta = \pi/4$. Concerning the dissipation error, the value $\text{Im}(\tilde{k}\Delta) = -6 \times 10^{-5}$ is obtained from the slope of the linear regression line in Fig. 10(b). It is equal to the theoretical value of $\text{Im}(k^*\Delta)$ which is found from Fig. 7 for $N = 8$ and $k\Delta = \pi/4$. In this case, the wavenumber obtained in the test case is the effective wavenumber, and the leading mode is the physical mode. The time variations of $\arg(p)$ and $\log|p|$ are now represented in Fig. 11 for an initial wave with wavenumber $k\Delta = 5\pi/8$, for which the solutions at the initial and final times are displayed in Fig. 9. It is seen that the phase of p is approximately a piecewise linear function of time. The logarithm of $|p|$ has different short-time and long-time behaviors. For $t < 20\Delta$, the slopes of $\arg(p)$ and $\log|p|$ correspond to the real and imaginary parts of the effective wavenumber. Therefore, the leading mode is the physical mode for $t < 20\Delta$. However, it is strongly attenuated and its amplitude is negligible at long time compared to that of the numerical modes. For $t > 20\Delta$, different numerical modes are dominant at various times. In addition, the estimated value of $\text{Re}[\tilde{k}\Delta]$ at long time from Fig. 11(a) is -0.4 . This is consistent with the solution at the final time displayed in Fig. 9(b) for $k\Delta = 5\pi/8$, whose wavenumber is smaller than that of the initial wave. The imaginary part of the wavenumber deduced from the linear regression line in Fig. 11(b) is equal to $\text{Im}[\tilde{k}\Delta] = -2 \times 10^{-3}$. This value is two order of magnitude smaller than $\text{Im}[k^*\Delta]$, as the amplitude of the leading mode decays less rapidly than that of the physical mode.

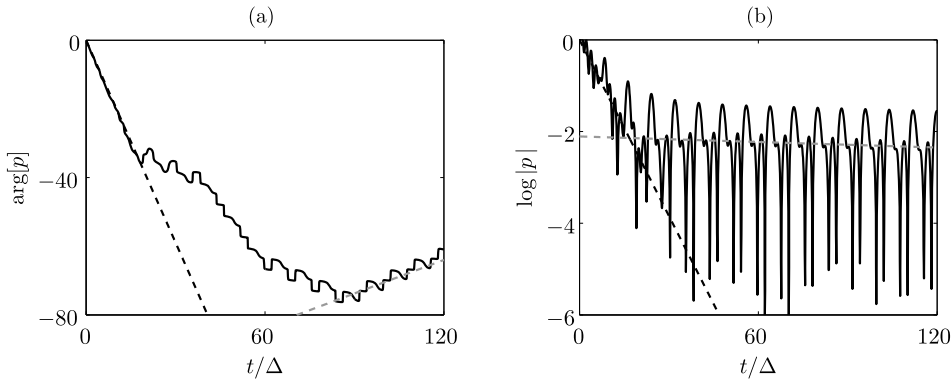


Fig. 11. Time variation of (a) the phase of p and (b) of the logarithm of $|p|$ for $k\Delta = 5\pi/8$ and for $N = 8$: — numerical solution, - - physical mode $p(t) \propto \exp(-ik^*t)$ and - · - linear regression line at long time.

Fig. 12 shows the real and imaginary parts of the wavenumbers associated with the different modes obtained for $N = 8$ from the theoretical analysis conducted above as a function of the exact wavenumber $k\Delta$. As discussed in the previous section, for $N = 8$, the wavenumbers associated with the numerical modes correspond to the effective wavenumber shifted along the $k\Delta$ -axis by multiples of $2\pi/N$. The wavenumbers obtained numerically are also represented by dots. For low wavenumbers, $k\Delta < \pi/2$, the real and imaginary parts of the wavenumbers estimated in the test case are in good agreement with those of the effective wavenumber, indicating that the leading mode is the physical mode. At higher wavenumbers, the estimated wavenumber does not correspond to the effective wavenumber but is related to numerical modes, as observed previously for $k\Delta = 5\pi/8$. In particular, for $k\Delta$ close to π , the real and imaginary parts of the estimated wavenumber are clearly superimposed on those of a wavenumber associated with a numerical mode.

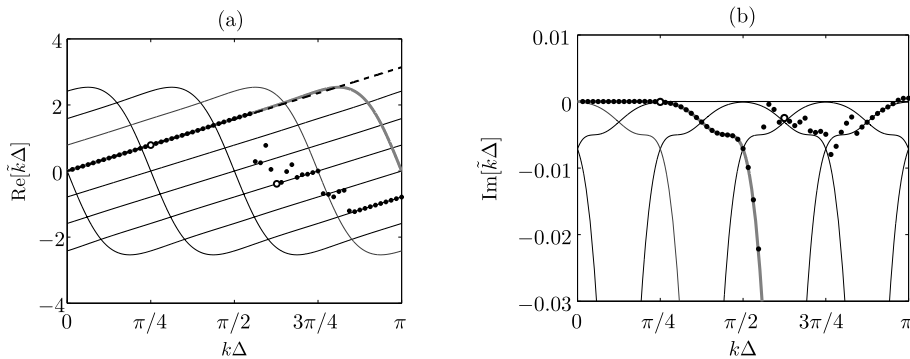


Fig. 12. (a) Real and (b) imaginary parts for $N = 8$ — of the effective wavenumber, — of the wavenumbers associated with the numerical modes, and • of the wavenumbers obtained in the test cases, as functions of the exact wavenumber $k\Delta$. The values obtained for $k\Delta = \pi/4$ and $k\Delta = 5\pi/8$ are represented by white dots.

2.4. Accuracy limits and numerical cost

To further quantify and compare the dispersion and dissipation errors, limits of accuracy are evaluated using the arbitrary criteria $|\text{Re}(k^*\Delta) - k\Delta|/\pi \leq \epsilon$ and $|1 - \exp[\text{Im}(k^*\Delta)]| \leq \epsilon$, where the threshold value is set to $\epsilon = 10^{-4}$. The accuracy limits for the dispersion and the dissipation errors are respectively expressed in terms of number of points per wavelength by λ_ϕ/Δ and λ_A/Δ . They are displayed in Fig. 13, as functions of N . The curves follow a downward trend with increasing N , converging toward $\lambda = \pi\Delta$. Values of the accuracy limits are given in Table 1. The accuracy limits are equal to 7.7 points per wavelength for $N = 8$, 5.2 for $N = 16$ and 4.0 for $N = 32$. For large values of $N > 64$, 3.5 points per wavelength are sufficient to obtain accurate results, in agreement with the suggestions of Boyd [8].

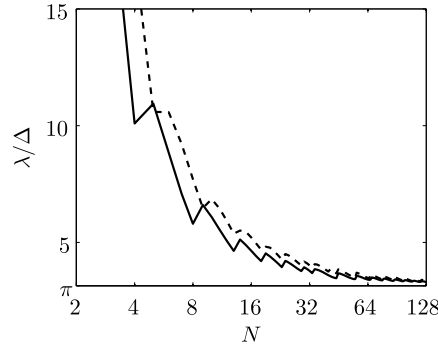


Fig. 13. Accuracy limits in term of λ/Δ , as functions of N , obtained for — the dispersion error and - - the dissipation error.

Table 1

Accuracy limits in term of number of points per wavelength for the dispersion error λ_ϕ/Δ and for the dissipation error λ_A/Δ for different values of N .

N	4	8	16	32	64	128	256
λ_ϕ/Δ	10.1	5.8	4.6	3.8	3.4	3.3	3.2
λ_A/Δ	17.4	7.7	5.2	4.0	3.5	3.3	3.2

The computation of the spatial derivative using the Chebyshev PS method is usually done through a matrix multiplication method for small N and through Fast Fourier Transform (FFT) for large N [8]. For the matrix multiplication method, the computational cost is typically of the order of N^2 . The cost per point is then proportional to $p = N$. For the FFT method, the computational cost for N points can be roughly estimated as $N \ln N$. The computational cost per point is then proportional to $p = \ln N$. More complex formula for the computational cost for the FFT [26] can be used, but results lead to the same conclusions. Moreover, the accuracy limits determined above correspond to the number of grid points required to obtain a given accuracy. The numerical efficiency for both methods can thus be estimated by multiplying the accuracy limits by the computational cost per point p . The lower the value of $p\lambda/\Delta$, the more efficient the Chebyshev PS method. Note that the efficiencies of the FFT method and the matrix multiplication method are not compared because, as shown by Fornberg [1] and Boyd [8], they are highly hardware and software dependent. Fig. 14 shows the values of $p\lambda/\Delta$ with N . All the curves first decrease, reach a minimum and then increase with N . For the matrix multiplication method, in Fig. 14(a), the minimum is found between $N = 4$ and $N = 8$. For the FFT method, in Fig. 14(b), the maximum efficiency is obtained for

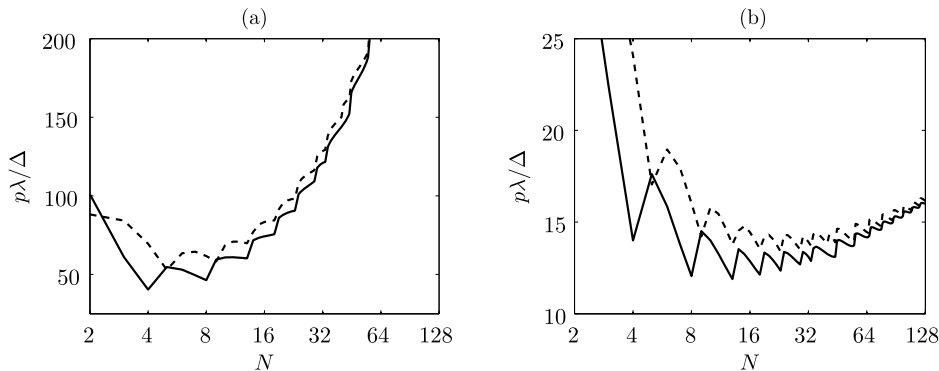


Fig. 14. Numerical efficiency $p\lambda/\Delta$, as a function of N , (a) for the matrix multiplication method with $p = N$ and (b) for the FFT method with $p = \ln N$: — $\lambda/\Delta = \lambda_\phi/\Delta$ and - - $\lambda/\Delta = \lambda_A/\Delta$.

larger values of N . The minimum of $p\lambda/\Delta$ is reached between $N = 16$ and $N = 32$. In all cases, it is worthwhile noting that the maximum efficiency is not obtained for infinite N , but for moderate values of N . This means that it is more suitable in term of computational cost to use subdomains than a single domain with a very large number of points. In addition, for the same average mesh size, the time step Δt decreases with increasing N [27,28], as shown in Section 2.5 for the fourth-order Runge–Kutta algorithm, also lowering the total efficiency for large subdomains.

2.5. Stability

The stability of the multi-domain PS Chebyshev method is now studied using the standard fourth-order explicit Runge–Kutta algorithm for the time integration. For that, the amplification factor, which is the rate of amplification of the solution between two consecutive time steps, is considered. For the s -stage Runge–Kutta algorithm, it is given [25] by:

$$G(\omega\Delta t) = 1 + \sum_{j=1}^s \gamma_j (-i\omega\Delta t)^j \quad (15)$$

where Δt is the time step and γ_j are the algorithm coefficients. Taking into account the dispersion equation $\tilde{k} = \omega/c$ for the 1-D advection equation, one obtains $\omega\Delta t = \text{CFL}\tilde{k}\Delta$ with the CFL number defined by $\text{CFL} = c\Delta t/\Delta$, where Δ is the average mesh size. Consequently, the amplification factor can be written as a function of the wavenumbers of the modes and of the CFL number, namely $G(\text{CFL}\tilde{k}\Delta)$. The multi-domain PS Chebyshev method is stable if $|G(\text{CFL}\tilde{k}\Delta)| \leq 1$ for all the wavenumbers \tilde{k} of the N modes. The maximal value of $|G|$ for all wavenumbers is represented in Fig. 15(a) as a function of the CFL number for different values of N between 4 and 32. At low CFL values, $|G|$ is almost equal to 1. If the time step exceeds a critical value, the amplification however increases rapidly. This critical value is a decreasing function of N , and is equal to 1.02 for $N = 4$, 0.70 for $N = 8$, 0.47 for $N = 16$ and 0.29 for $N = 32$. Fig. 15(b) shows the variation of $|G| - 1$ in logarithmic scales. It is noted that, even for small CFL numbers, the amplification rate can be larger than 1. Thus, for $N = 4$, this is the case for all CFL numbers. However, the amplification rate is very small, typically inferior to 2×10^{-3} , and the method is only weakly unstable. For large values of N , the maximum amplification rate for small CFL numbers is a decreasing function of N . For example, it is equal to 6×10^{-5} for $N = 16$ and 5×10^{-5} for $N = 32$. This behavior is due to the positive values of $\text{Im}[k^*\Delta]$ observed in Fig. 5(b) for a small range of wavenumbers. Finally, for some values of the CFL number, the multi-domain Chebyshev PS method is unconditionally stable. This is the case, for instance, for $N = 16$ and for CFL numbers between 0.32 and 0.45. For such values of CFL, the dissipation due to the time-integration scheme exceeds the amplification due to the spatial differentiation method.

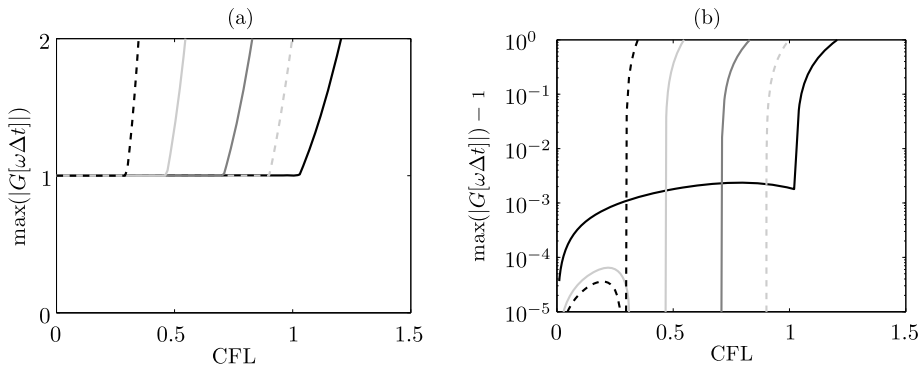


Fig. 15. Amplification rate per time step (a) in linear scale and (b) in logarithmic scale as a function of the CFL number using the standard fourth-order Runge–Kutta method, obtained for the multi-domain Chebyshev PS method for — $N = 4$, — $N = 8$, — $N = 16$ and — $N = 32$ and — for the Fourier PS method.

For the comparison, the amount of amplification for the Fourier PS method is shown in Fig. 15, assuming that the dispersion relation $\tilde{k} = k$ is verified for $k\Delta$ between 0 and π . As for the multi-domain Chebyshev PS method, $|G|$ is close to 1 for small CFL numbers, and increases abruptly for CFL numbers above a critical value, which is here equal to $\text{CFL} = 0.9$. It is observed that, the stability of the Fourier PS method is ensured for higher CFL numbers compared to the Chebyshev PS method with $N \geq 8$.

The generation of instabilities for large CFL numbers is now illustrated for the multi-domain Chebyshev PS method. As done previously, an initial harmonic wave with wavenumber $k\Delta = 3\pi/8$ is computed. The parameter N , related to the number of grid points ($N + 1$) in a subdomain, is set to 16. Two simulations are performed with CFL numbers just below and above the maximum value ensuring stability, which is $\text{CFL} = 0.47$ for $N = 16$. The solution is advanced over 25 time steps. The real part of the solution is plotted in Fig. 16(a) for $\text{CFL} = 0.44$ as a function of the normalized distance x/Δ . The numerical solution is in very good agreement with the analytical solution. In Fig. 16(b), the CFL number is increased to a value of 0.5. In this case, as expected, the numerical solution is strongly amplified at some points in the computational domain.

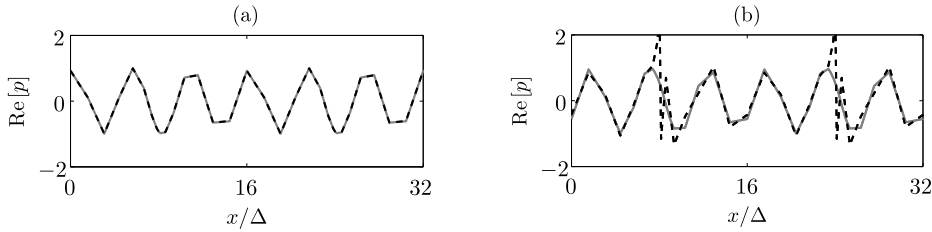


Fig. 16. Real part of — the analytical solution and of - - the numerical solution after 25 time steps as a function of x/Δ for $N = 16$ with $k\Delta = 3\pi/8$ (a) for $\text{CFL} = 0.44$ and (b) for $\text{CFL} = 0.50$.

The stability limit obtained for an amplification rate $|G(\text{CFL}\tilde{k}\Delta)| = 1.01$ is displayed in Fig. 17 as a function of N . As mentioned previously, the maximum CFL number ensuring the stability is a decreasing function with N . More precisely, it can be written as N^α with $-1 < \alpha < -1/2$. The parameter α is close to $-1/2$ for $N < 8$, but is close to -1 for $N > 128$. Interestingly, the maximum time step ensuring the stability of the multi-domain Chebyshev PS method here decreases as N^{-2} only for large N . For small N , it decreases less rapidly, typically as $N^{-3/2}$.

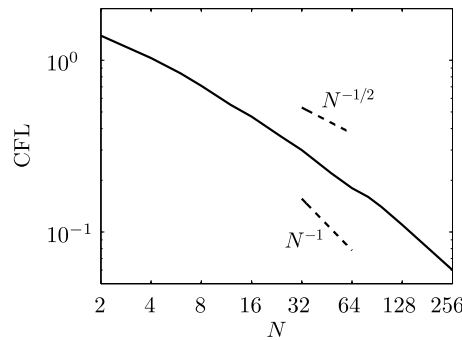


Fig. 17. Stability limit of the multi-domain Chebyshev PS method in term of the CFL number, as a function of N , using the standard fourth-order Runge–Kutta method.

3. Application to 1-D and 2-D problems

3.1. One-dimensional problem

A broadband one-dimensional wave propagation problem is first considered by solving the advection equation (1), with a propagation speed $c = 1$. The initial disturbances are given by:

$$p(x, t = 0) = \cos\left(\frac{2\pi x}{a\Delta}\right) \exp\left[-\ln 2 \left(\frac{x}{b\Delta}\right)^2\right] \quad (16)$$

where $a\Delta$ is the dominant wavelength and $b\Delta$ is the Gaussian half-width. As in the previous section, the parameter Δ denotes the average grid size. The computational domain is split into subdomains. The parameter N related to the number of points ($N + 1$) in the subdomains is set to $N = 8$, $N = 16$ or $N = 32$. Two values for the dominant wavelength $\lambda = a\Delta$ are considered. First, the dominant wavelength is chosen as $a\Delta = 6\Delta$. This value is below the accuracy limit given in Table 1 for $N = 8$, which is $\lambda/\Delta = 7.7$, and above those for $N = 16$ and $N = 32$, which are respectively $\lambda/\Delta = 5.2$ and $\lambda/\Delta = 4.0$. Numerical errors are thus expected to be significant for $N = 8$, but very small for $N = 16$ and $N = 32$. Second, the dominant wavelength is set to $a\Delta = 4.5\Delta$. According to Table 1, an accurate numerical solution is expected only for $N = 32$ in this case. In both cases, the Gaussian half-width is chosen as $b\Delta = 7\Delta$. The corresponding energy spectral densities are represented as a function of $k\Delta$ in Fig. 18.

The six-stage fourth-order Runge–Kutta algorithm of Berland et al. [25] is used for time integration. The CFL number is equal to 0.05, which is a very low value ensuring negligible time-integration error compared to spatial derivative errors.

The solutions obtained at $t = 100\Delta$ for $a = 6$ and $b = 7$ are plotted in Fig. 19 as a function of x/Δ . As expected, dissipation errors appear clearly in Fig. 19(a) for $N = 8$, whereas a good agreement is obtained with the analytical solution in Fig. 19(b) for $N = 16$. The solution obtained for $N = 32$ is not represented because it is very similar to the solution obtained for $N = 16$. The error with respect to the analytical solution p_{ana} is displayed in Fig. 20 for the different values of N as a function of x/Δ . The maximum error is in the order of 20% for $N = 8$, 1% for $N = 16$, and is lower than 0.01% over the whole computational domain for $N = 32$.

The solutions obtained at $t = 100\Delta$ for $a = 4.5$ and $b = 7$ are represented in Fig. 21 as a function of x/Δ . Large dispersion and dissipation errors are clearly seen in Fig. 21(a) for $N = 8$, whereas the agreement with the analytical solution is fair in

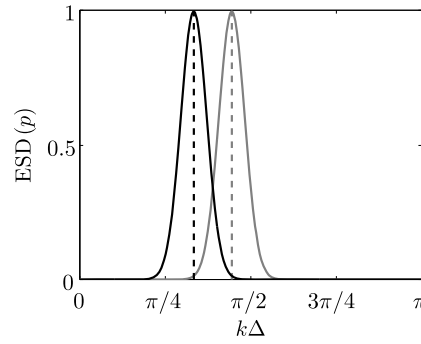


Fig. 18. Normalized energy spectral density of the initial disturbances p as a function of the exact wavenumber $k\Delta$ for: — $a = 6$ and $b = 7$, — $a = 4.5$ and $b = 7$.

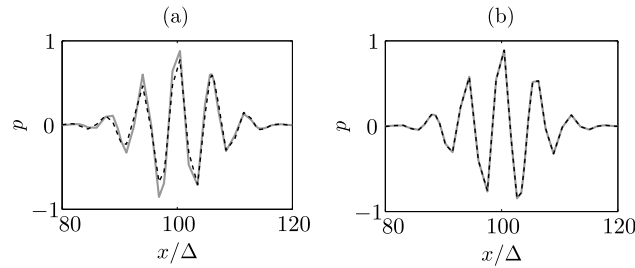


Fig. 19. Solutions obtained at $t = 100\Delta$ as functions of x/Δ for $a = 6$ and $b = 7$, (a) for $N = 8$ and (b) for $N = 16$: — analytical solution and - - numerical solution.

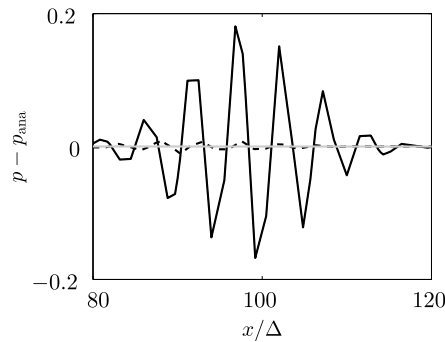


Fig. 20. Errors $p - p_{\text{ana}}$ obtained at $t = 100\Delta$ as functions of x/Δ for $a = 6$ and $b = 7$, for — $N = 8$, - - $N = 16$ and — $N = 32$.

Fig. 21(b) for $N = 16$. In the latter case, however, the amplitude of the numerical solution is lower than that of the analytical one due to dissipation error. Finally, the numerical solution is superimposed on the analytical solution in Fig. 21(c) for $N = 32$. The error $p - p_{\text{ana}}$ is shown in Fig. 22 for the three values of N as a function of x/Δ . The maximum error is very large for $N = 8$, typically of 70%, is equal to 10% for $N = 16$ and is reduced to 0.1% for $N = 32$.

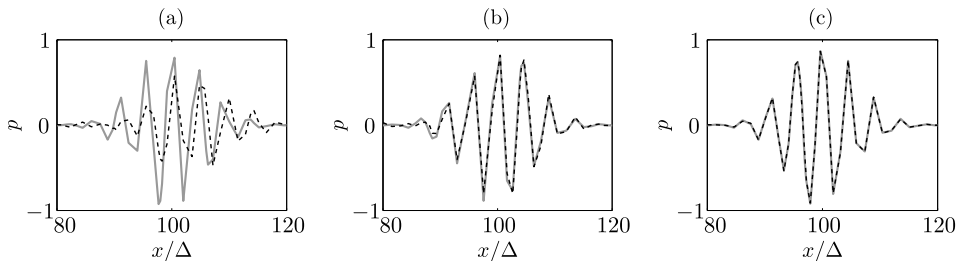


Fig. 21. Solutions obtained at $t = 100\Delta$ as a function of x/Δ for $a = 4.5$ and $b = 7$, (a) for $N = 8$, (b) for $N = 16$ and (c) for $N = 32$: — analytical solution and - - numerical solution.

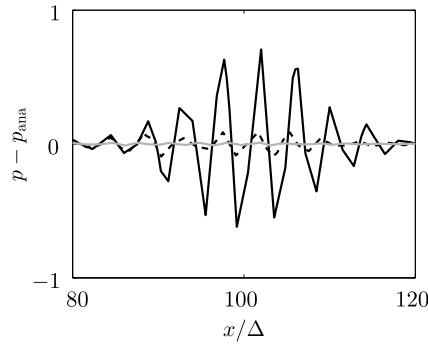


Fig. 22. Errors $p - p_{\text{ana}}$ obtained at $t = 100\Delta$ as functions of x/Δ for $a = 4.5$ and $b = 7$, for $N = 8$, $N = 16$ and $N = 32$.

3.2. Two-dimensional problem and hybrid Fourier–Chebyshev PS method

The accuracy of numerical solutions for multi-dimensional problems can exhibit anisotropy, even if the considered equations are isotropic. This has been demonstrated for instance for low-order finite-difference schemes for short wavelengths [29,30]. To explain the origin of anisotropy simply, a two-dimensional plane wave with an angular frequency ω and a wavenumber $\mathbf{k} = (k \cos \theta, k \sin \theta)$ propagating at an angle θ is considered. In the system of coordinates $\mathbf{r} = (x, y)$, it is written as:

$$\exp(i\mathbf{k} \cdot \mathbf{r} - i\omega t) = \exp(ik \cos \theta x) \exp(ik \sin \theta y) \exp(-i\omega t) \quad (17)$$

The derivative operator in the x - and y -directions applies here to waves with wavenumbers equal to $k \cos \theta$ and $k \sin \theta$ respectively. It was shown in the previous section that the error due to the spatial derivative operator generally reduces with decreasing wavenumbers. Therefore, the global error is expected to be maximal for waves propagating along the grid directions, where the corresponding wavenumbers are the highest. Conversely, the global error is expected to be minimal for waves propagating in the diagonals of the grid, where the wavenumbers in the grid directions are minimal.

As shown, in Section 2, the numerical errors introduced by the Chebyshev PS method can be large for small wavelengths and for moderate values of N . Therefore, the error anisotropy is also expected to be significant for the Chebyshev PS method. Besides, various derivative operators can be implemented in the different spatial directions. This is the case for hybrid Fourier–Chebyshev PS solvers [31–33]. The idea is to use a Fourier PS method in the periodic directions and a Chebyshev PS method for the other directions. For short waves, the Fourier PS method is however more accurate than the Chebyshev PS method using moderate values of N . One can then wonder if accurate results are still obtained in the grid direction using the Fourier PS method or if the errors are important in all directions.

In this section, the propagation of cylindrical waves is considered to study the variations of the numerical error with the propagation angle. The linearized Euler equations without mean flow are solved:

$$\frac{\partial p}{\partial t} + \nabla \cdot \mathbf{v} = 0 \quad (18)$$

$$\frac{\partial \mathbf{v}}{\partial t} + \nabla p = 0 \quad (19)$$

The initial disturbances are:

$$p(\mathbf{r}, t = 0) = J_0\left(\frac{2\pi r}{a\Delta}\right) \exp\left[-\ln 2 \left(\frac{r}{b\Delta}\right)^2\right] \quad (20)$$

The analytical solution is given by [22]:

$$p_{\text{ana}}(\mathbf{r}, t) = \frac{1}{2\pi} \int_0^{+\infty} H(k) J_0(kr) \cos(kt) k dk \quad (21)$$

where $H(k)$ is the Hankel transform of the initial disturbances. Denoting $b' = b/\sqrt{\ln 2}$, it is written as:

$$H(k) = \pi b'^2 \Delta^2 \exp\left[-\left(k\Delta - \frac{2\pi}{a}\right)^2 \frac{b'^2}{4}\right] \exp\left(-\frac{k\Delta\pi b'^2}{a}\right) I_0\left(\frac{k\Delta\pi b'^2}{a}\right) \quad (22)$$

where I_0 is the modified Bessel function of the first kind of order 0. The above relation is obtained by using the Weber's second exponential integral [34]. For sufficiently large $k\Delta \gg a/(b'^2 4\pi)$, the term $H(k)$ can be expressed as:

$$H(k) \approx b' \Delta^2 \sqrt{\frac{a}{2k\Delta}} \exp \left[- \left(k\Delta - \frac{2\pi}{a} \right)^2 \frac{b'^2}{4} \right] \quad (23)$$

As for the one-dimensional wave defined by (16), the parameters a and b provide the dominant wavelength and the pulse bandwidth, respectively. The values $a = 2\pi$ and $b = 3\pi/2$ are chosen to obtain a broadband signal with frequency contents up to the wavenumber $k\Delta = 2$, as shown in Fig. 23.

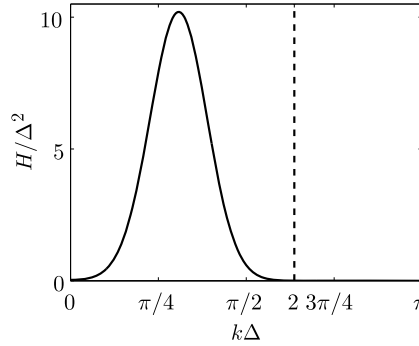


Fig. 23. Normalized Hankel transform $H(k)$ of the initial pressure distribution for $a = 2\pi$ and $b = 3\pi/2$, as a function of the exact wavenumber $k\Delta$.

Three computations, referred to as FF, CCN and FCN, are performed. In the FF and CCN cases, Fourier and Chebyshev PS methods are used in both x - and y -directions, respectively. In the first case, the number of points is $N_F = 800$, whereas in the second case the multi-domain Chebyshev PS method is used with $N = 8$, $N = 16$ or $N = 32$ in the subdomains. Finally, in the FCN computation, Fourier PS method is used in the x -direction with $N_F = 800$ points, and a multi-domain Chebyshev PS method is implemented in the y -direction with $N = 16$. The mesh size in the directions using the Fourier PS method is fixed to $\Delta_F = \pi\Delta/2$, because waves are accurately computed down to 2 points per wavelength.

The time step is equal to $\Delta t = 0.05\Delta$. The six-stage fourth-order Runge–Kutta algorithm of Berland et al. [25] is employed for the time integration. The perfectly matched layer [35] boundary conditions are used in the splitting form at the outer boundaries to ensure minimum reflection. At the interfaces of the Chebyshev subdomains, the method of the characteristic variables is applied, as done for instance by Carcione [36]. In order to evaluate the error anisotropy, a circle of receivers is located at a distance $R_c = 200\Delta$ from the center of the initial disturbance. The simulation is run up to a final time $t = 400\Delta$, and the error is computed as a function of the wave propagation angle θ using the relation:

$$E_2(\theta) = \sqrt{\frac{\int_0^t [p(R_c, \theta, t') - p_{\text{ana}}(R_c, t')]^2 dt'}{\int_0^t p_{\text{ana}}(R_c, t')^2 dt'}} \quad (24)$$

where p_{ana} is the analytical solution.

The errors E_2 computed from the simulations FF and CC32 are shown in Fig. 24 for angle $\theta \in [0, \pi/2]$ because of the symmetries of the problem. The peak error values are approximately of 0.04% for FF, and of 0.3% for CC32, which is small. This demonstrates that using $N = 32$ in the Chebyshev subdomains allows to obtain accurate results. Using Fourier PS method in both x - and y -directions visibly leads to an isotropic error, suggesting that the error due to the spatial differentiation is lower than that due to the time integration. To support this claim, an additional simulation is performed using the Fourier PS method with a time step divided by two. As found in Fig. 24, the error obtained is still isotropic but

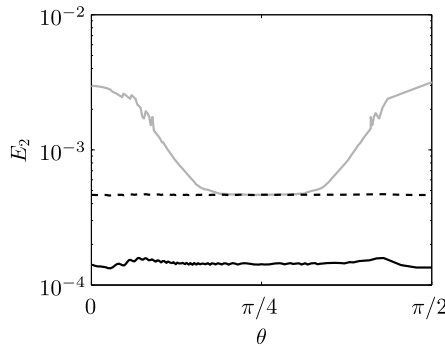


Fig. 24. Error E_2 in logarithmic scale relative to the analytical solution evaluated at the distance $R_c = 200\Delta$ as a function of the angle θ from — CC32: Chebyshev PS method used in both grid directions with $N = 32$, -- FF: Fourier PS method used in both grid directions and — FF($\Delta t/2$): the same as FF with a time step divided by two.

its value is lowered to 0.015%. Concerning the simulation CC32, the error is observed to vary with θ , and to be maximum in the grid directions, as expected. Note also that close to the direction $x = y$, where $\theta = \pi/4$, the error is comparable to that obtained in the FF simulation.

We now examine the angular variations of the errors for the computations CCN. The errors with respect to the analytical solution E_2 are represented in Fig. 25 in logarithmic scale for $N = 8$, $N = 16$ and $N = 32$ as a function of the angle θ . In all cases, the peak error is observed along the grid directions. With respect to the CC32 simulation, the maximum error is respectively two and one orders of magnitude larger for the simulations CC8 and CC16. More precisely, it is equal to 37.9% for the CC8 case, to 4.4% for the CC16 case, and to 0.3% for the CC32 case. Numerical and analytical solutions obtained at $\theta = 0$ are represented in Fig. 26(a) as a function of the normalized time t/Δ . Compared to the analytical solution, the amplitude of the wave is significantly lower in CC8. The solutions obtained for the simulations CC16 and CC32 are in good agreement with the analytical solution. The time variations of the error $p - p_{\text{ana}}$ obtained at $\theta = 0$ are displayed in Fig. 26(b). Maximum error values are equal to 9×10^{-3} for CC8, 7×10^{-4} for CC16 and 5×10^{-5} for CC32. In addition, oscillations with periods smaller than 5Δ are observed for $N = 8$. For $N = 16$, some oscillations with a smaller amplitude and with a period close to 4Δ are also noticed. It can be remarked that the wavelengths corresponding to the periods of these oscillations are below the accuracy limits given in Table 1 in Section 2.4.

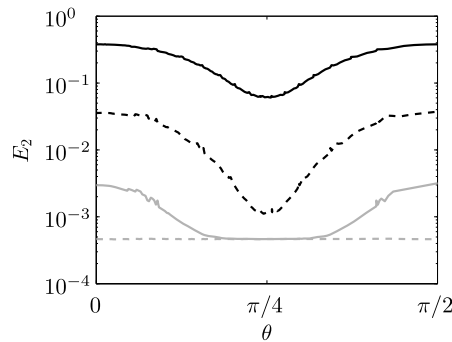


Fig. 25. Error E_2 in logarithmic scale relative to the analytical solution evaluated at the distance $R_C = 200\Delta$ as a function of the angle θ obtained for simulations in which Chebyshev PS method is used in both directions — CC8 with $N = 8$, - - CC16 with $N = 16$ and — CC32 with $N = 32$ and for - - simulation FF.

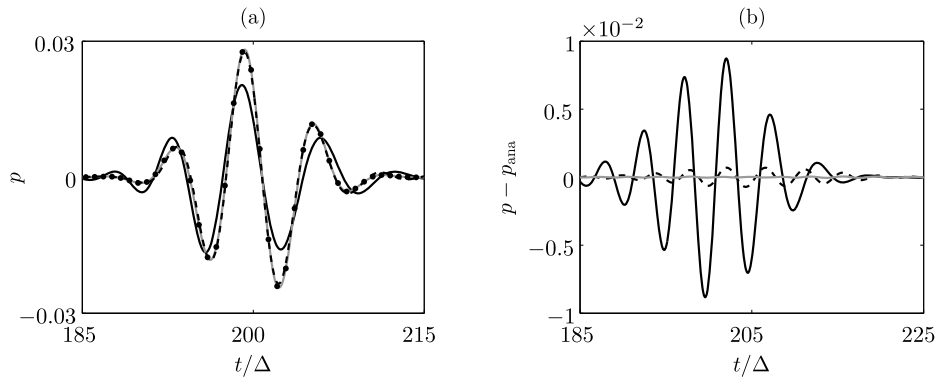


Fig. 26. (a) Solutions and (b) errors $p - p_{\text{ana}}$ evaluated at the distance $R_C = 200\Delta$ as functions of t/Δ : • analytical solution and numerical solutions for $\theta = 0$ obtained from — CC8, - - CC16 and — CC32.

The error anisotropy for the hybrid Fourier–Chebyshev PS solver is now examined. The variations of the errors obtained in the simulation FC16 relative to the analytical solution are represented in Fig. 27 as functions of the angle θ . For the comparison, the errors obtained in the simulations FF and CC16, in which the Fourier PS method and the Chebyshev PS method with $N = 16$ are used in both directions, respectively, are also plotted. In the x -direction, for $\theta \simeq 0$, the errors are close to those obtained in the simulation FF. Moreover, they do not depend significantly on the propagation angle for $\theta \lesssim \pi/4$. In the y -direction, for $\theta \simeq \pi/2$, the variations of the errors with θ are very similar to those obtained in CC16. The solutions obtained in FC16 along the x -direction for $\theta = 0$ and along the y -direction for $\theta = \pi/2$ are shown in Fig. 28(a) as a function of the normalized time t/Δ . A good agreement with the analytical solution is obtained in both directions. The time variations of the error with respect to the analytical solution are represented in Fig. 28(b). Along the x -direction, it is very small, and is lower than 2×10^{-5} . Along the y -direction, the error is comparable to that obtained in Fig. 26(b) in CC16 and its peak value is 7×10^{-4} . Thus, one can expect that, for hybrid Fourier–Chebyshev computations, waves propagating

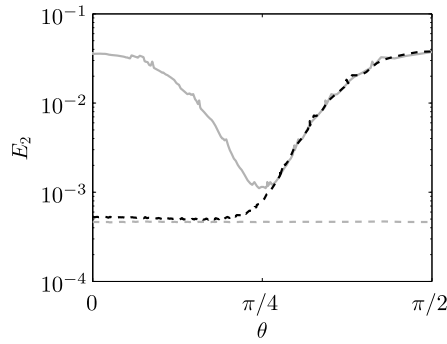


Fig. 27. Error E_2 in logarithmic scale relative to the analytical solution evaluated at the distance $R_C = 200\Delta$ as a function of the angle θ for simulations — CC16, - - FF and - · - FC16: Fourier PS method used in the x -direction and Chebyshev PS method with $N = 16$ used in the y -direction.

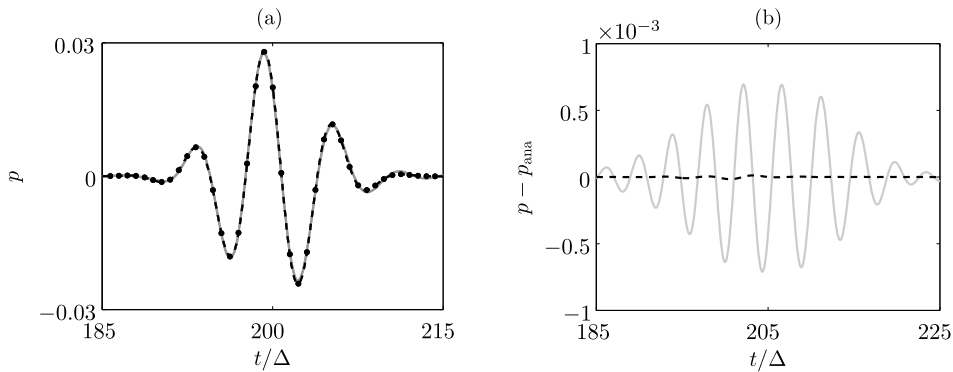


Fig. 28. (a) Solutions and (b) errors $p - p_{ana}$ evaluated at the distance $R_C = 200\Delta$ as functions of t/Δ : • analytical solution and numerical solutions obtained from FC16 — along the x -direction for $\theta = 0$ and — along the y -direction for $\theta = \pi/2$.

in the grid direction along which the Fourier PS method is implemented are accurately resolved down to the limit of two points per wavelength. Only waves propagating in the grid directions along which the Chebyshev PS method is used suffer from reduced accuracy for short wavelengths.

4. Conclusions

A detailed analysis on the numerical errors generated by the multi-domain Chebyshev pseudospectral method is carried out. An eigenvalue problem is formulated by considering harmonic-wave type solutions of the 1-D advection equation. Among the eigenmodes, one corresponds to the physical solution. The dispersion and dissipation errors associated to the eigenvalue of the physical mode are investigated, depending on the number of points $(N + 1)$ in the subdomains. For values of N used in the literature for the multi-domain Chebyshev PS approach, typically $N = 8$ to $N = 32$, it is shown that accuracy is poor for short wavelengths. The theoretical values of the dispersion and dissipation errors compare very well with those obtained in numerical test cases. Accuracy limits, based on arbitrary criteria on the dispersion and dissipation errors, are then proposed for long-range wave propagation problems. It is found that 7.7, 5.2 and 4.0 points per wavelength are at least needed for $N = 8, 16, 32$ respectively to obtain a satisfactory accuracy at long range. For N larger than typically 64, a resolution of 3.5 points per wavelength is sufficient. It is concluded that, from a numerical efficiency point of view, it is preferable for common applications to use multi-domains with N between 16 to 32 rather than a single domain with a large number of points.

Furthermore, the stability of the method is examined using the standard fourth-order Runge–Kutta algorithm. For large N , the maximum time step ensuring the stability decreases as N^{-2} . The stability constraint is less restrictive for small N , as the time step decreases as $N^{-3/2}$. It is shown that the stability of the Fourier PS method is ensured at higher CFL numbers compared to the multi-domain Chebyshev PS method for $N \geq 6$.

Finally, 1-D and 2-D problems are considered to emphasize the dispersion and dissipation errors for short waves. In a 2-D geometry, anisotropy of the solutions is exhibited, in particular for a hybrid Fourier–Chebyshev PS configuration. The reduced accuracy of the Chebyshev PS method is observed only for waves propagating in the grid direction along which this method is implemented. Close to the grid direction along which the Fourier PS method is applied, the error is comparable with that obtained from a full Fourier PS configuration. Applications of the hybrid Fourier–Chebyshev PS configuration for long-range sound propagation in the atmosphere will be reported in future publications.

References

- [1] B. Fornberg, A Practical Guide to Pseudospectral Methods, Cambridge University Press, 1996.
- [2] D. Kosloff, E. Baysal, Forward modeling by a Fourier method, *Geophysics* 47 (10) (1982) 1402–1412.
- [3] Q.H. Liu, The PSTD algorithm: A time-domain method requiring only two cells per wavelength, *Microw. Opt. Technol. Lett.* 15 (3) (1997) 158–165.
- [4] E. Filoux, S. Callé, D. Certon, M. Lethiecq, F. Levassort, Modeling of piezoelectric transducers with combined pseudospectral and finite-difference methods, *J. Acoust. Soc. Am.* 123 (6) (2008) 4165–4173.
- [5] W.H.P. Pernice, Pseudo-spectral time-domain simulation of the transmission and the group delay of photonic devices, *Opt. Quantum Electron.* 40 (2008) 1–12.
- [6] X. Huang, X. Zhang, A Fourier pseudospectral method for some computational aeroacoustics problems, *Int. J. Aeroacoust.* 5 (3) (2006) 279–294.
- [7] M. Hornikx, R. Waxler, J. Forssén, The extended Fourier pseudospectral time-domain (PSTD) method for fluid media with discontinuous properties, *J. Comput. Acoust.* 18 (4) (2010) 297–319.
- [8] J.P. Boyd, *Chebyshev and Fourier Spectral Methods*, Dover Publications, 2001.
- [9] L.N. Trefethen, *Spectral Methods in MATLAB*, SIAM, 2000.
- [10] Y. Ha, K. Lee, W. Seong, Pseudospectral time-domain method for pressure-release rough surface scattering using a surface transformation and image method, *Numer. Algorithms* 54 (2010) 411–430.
- [11] M. Hornikx, R. Waxler, J. Forssén, The extended Fourier pseudospectral time-domain method for atmospheric sound propagation, *J. Acoust. Soc. Am.* 128 (4) (2010) 1632–1646.
- [12] J.S. Hesthaven, P.G. Dinesen, J.P. Lynov, Spectral collocation time-domain modeling of diffractive optical elements, *J. Comput. Phys.* 155 (1999) 287–306.
- [13] G. Zhao, Q.H. Liu, The 2.5-D multidomain pseudospectral time-domain algorithm, *IEEE Trans. Antennas Propag.* 51 (3) (2003) 619–627.
- [14] M. Dehghan, A. Taleei, A Chebyshev pseudospectral multidomain method for the soliton solution of coupled nonlinear Schrödinger equations, *Comput. Phys. Commun.* 182 (2011) 2519–2529.
- [15] F.Q. Hu, M.Y. Hussaini, P. Rasetarinera, An analysis of the discontinuous Galerkin method for wave propagation problems, *J. Comput. Phys.* 151 (1999) 921–946.
- [16] G. Gassner, D.A. Kopriva, A comparison of the dispersion and dissipation errors of Gauss and Gauss–Lobatto discontinuous Galerkin spectral element methods, *SIAM J. Sci. Comput.* 33 (5) (2011) 2560–2579.
- [17] T. Melvin, A. Staniforth, J. Thuburn, Dispersion analysis of the spectral element method, *Q. J. R. Meteorol. Soc.* 138 (2012) 1934–1947.
- [18] K. Van den Abeele, C. Lacor, Z.J. Wang, On the stability and accuracy of the spectral difference method, *J. Sci. Comput.* 37 (2008) 162–188.
- [19] K. Van den Abeele, T. Broeckhoven, C. Lacor, Dispersion and dissipation properties of the 1D spectral volume method and application to a p -multigrid algorithm, *J. Comput. Phys.* 224 (2007) 616–636.
- [20] D.A. Kopriva, Spectral solution of acoustic wave-propagation problems, in: Thirteenth AIAA Aeroacoustics Conference, Tallahassee, FL, USA, 1990, AIAA Paper 1990-3916.
- [21] C.E. Wasberg, D. Gottlieb, Optimal decomposition of the domain in spectral methods for wave-like phenomena, *SIAM J. Sci. Comput.* 22 (2) (2000) 617–632.
- [22] C.K.W. Tam, J.C. Webb, Dispersion-relation preserving finite difference schemes for computational acoustics, *J. Comput. Phys.* 107 (1993) 262–281.
- [23] S.K. Lele, Compact finite difference schemes with spectral-like resolution, *J. Comput. Phys.* 103 (1992) 16–42.
- [24] C. Bogey, C. Bailly, A family of low dispersive and low dissipative explicit schemes for flow and noise computations, *J. Comput. Phys.* 194 (2004) 194–214.
- [25] J. Berland, C. Bogey, C. Bailly, Low-dissipation and low-dispersion fourth-order Runge–Kutta algorithm, *Comput. Fluids* 35 (2006) 1459–1463.
- [26] S.G. Johnson, M. Frigo, A modified split-radix FFT with fewer arithmetic operations, *IEEE Trans. Signal Process.* 55 (1) (2007) 111–119.
- [27] D. Gottlieb, J.S. Hesthaven, Spectral methods for hyperbolic problems, *J. Comput. Appl. Math.* 128 (1–2) (2001) 83–131.
- [28] D. Gottlieb, S.A. Orszag, *Numerical Analysis of Spectral Methods*, SIAM, 1977.
- [29] C.K.W. Tam, J.C. Webb, Radiation boundary condition and anisotropy correction for finite difference solutions of the Helmholtz equation, *J. Comput. Phys.* 113 (1994) 122–133.
- [30] A. Sescu, R. Hixon, A.A. Afjeh, Multidimensional optimization of finite difference schemes for computational aeroacoustics, *J. Comput. Phys.* 227 (2008) 4563–4588.
- [31] E. Tessmer, D. Kessler, D. Kosloff, A. Behle, Multi-domain Chebyshev–Fourier method for the solution of the equations of motion of dynamic elasticity, *J. Comput. Phys.* 100 (1992) 355–363.
- [32] B.-Y. Guo, J. Li, Fourier–Chebyshev pseudospectral method for two-dimensional vorticity equation, *Numer. Math.* 66 (1993) 329–346.
- [33] R. Sidler, J.M. Carcione, K. Holliger, A pseudo-spectral method for the simulation of poro-elastic seismic wave propagation in 2D polar coordinates using domain decomposition, *J. Comput. Phys.* 235 (2013) 846–864.
- [34] G.N. Watson, *Theory of Bessel Functions*, Cambridge University Press, 1922.
- [35] J.P. Bérenger, A perfectly matched layer for the absorption of electromagnetic waves, *J. Comput. Phys.* 114 (1994) 185–200.
- [36] J.M. Carcione, A 2-D Chebyshev differential operator for the elastic wave equation, *Comput. Methods Appl. Mech. Eng.* 130 (1996) 33–45.